Phononic Crystal Cavity Magnomechanics

Daiki Hatanaka,* Motoki Asano, Hajime Okamoto, and Hiroshi Yamaguchi
NTT Basic Research Laboratories, NTT Corporation, Atsugi-shi, Kanagawa 243-0198, Japan

(Received 16 November 2022; revised 8 March 2023; accepted 17 April 2023; published 22 May 2023)

Phononic crystal (PnC) enables strong confinement of phonons in a wavelength-scale tiny area due to a band gap, which can enhance the interaction with different physical systems. Here, we utilize the PnC to demonstrate local manipulations of magnons by using ultrahigh frequency phonons confined in a phononic cavity, where the tiny and low-loss vibrations excite magnons in a micromagnet via magnetostriction. Moreover, we find that the magnetoelastic interaction is modulated by selectively exciting the cavity resonant modes. The results open up a realm of PnC cavity magnomechanics and will provide universal controls of ultrahigh frequency magnons and phonons with PnC circuits.

DOI: 10.1103/PhysRevApplied.19.054071

I. INTRODUCTION

Magnonics is increasingly relevant from the viewpoints of both fundamental study and technological applications because of the unique properties of magnons, such as nanometer wavelengths, wide frequency range from GHz to low THz, high tunability, and Joule heat-free propagation [1,2]. Their use as information carriers holds promise for developing compact, high-speed, and low-power-consumption devices for wireless telecommunications and hardware-based neuromorphic computing as well as studying quantum information technology [3–11]. The ability to manipulate them has relied on Oersted fields generated from electromagnetic waves in a metallic stripline and cavity resonator. The excitation efficiency of magnons from microwave photons is governed by a quality factor to volume ratio (Q/V) of an electromagnetic system, which is well known in the field of cavity quantum electrodynamics [12]. However, those systems host insufficient Q/V due to the millimeter-scale structure (large V), and/or inevitable radiation loss and crosstalks (low Q). Thus, despite expectations, the magnonics systems have been energetically inefficient and have had poor scaling behaviors.

Acoustic phonons at microwave frequencies are promising candidates for an alternative interface with magnons because of their micro- and nanometer wavelength and negligible radiation loss [10,11,13–16]. The use of an appropriate phononic platform for a magnomechanical system enables local and efficient excitation of microscopic magnons with spatially controlled phonons via the magnetoelastic effect. A phononic crystal (PnC) enables acoustic phonons to be guided and trapped in a wavelength-scale acoustic cavity and waveguide [17–24]. Individual cavities have ultrasmall V and high Q and realize 10^4–10^5 times higher Q/V than conventional surface acoustic wave (SAW) systems [25–33]. Therefore, they can be used to efficiently control micrometer and even nanometer-scale magnetic elements and magnons embedded in a PnC circuit. Thus, the PnC is a promising platform to make full use of phonons in a magnomechanical system.

Here, we demonstrate a PnC-based magnomechanical system sustained by phononic cavity-waveguide coupled systems, as shown in Fig. 1(a). The nanomechanical vibrations confined in the PnC cavity, excited through the waveguide, generate spin waves (magnons) in a nickel (Ni) film placed on its surface via magnetostriction. The acoustic spin pumping reversibly induces a frequency shift and damping modulation of the phononic cavity resonances. Moreover, the spatial phononic confinement by the PnC cavity generates various strain distributions of cavity modes and enables the magnon-phonon interaction to be tailored by selectively driving an appropriate mode. The integration of the phononics technology into magnomechanics opens up a realm of PnC cavity magnomechanics, which provides an alternative approach for dynamic and spatial controls of microscopic magnons and phonons.

II. RESULTS

A. Device

The PnC consists of a snowflake triangular lattice with full band gaps between 0.4 and 0.7 GHz [Figs. 1(b)–1(d)] [24,34]. Acoustic waves at frequencies within the band gap propagate in a line-defect waveguide and drive a PnC cavity with a two-hole defect, where a Ni film is deposited to form a magnon-phonon coupled system. Measuring the spectral response of the PnC cavity with an optical interferometer reveals three acoustic resonances

*daiki.hatanaka@ntt.com

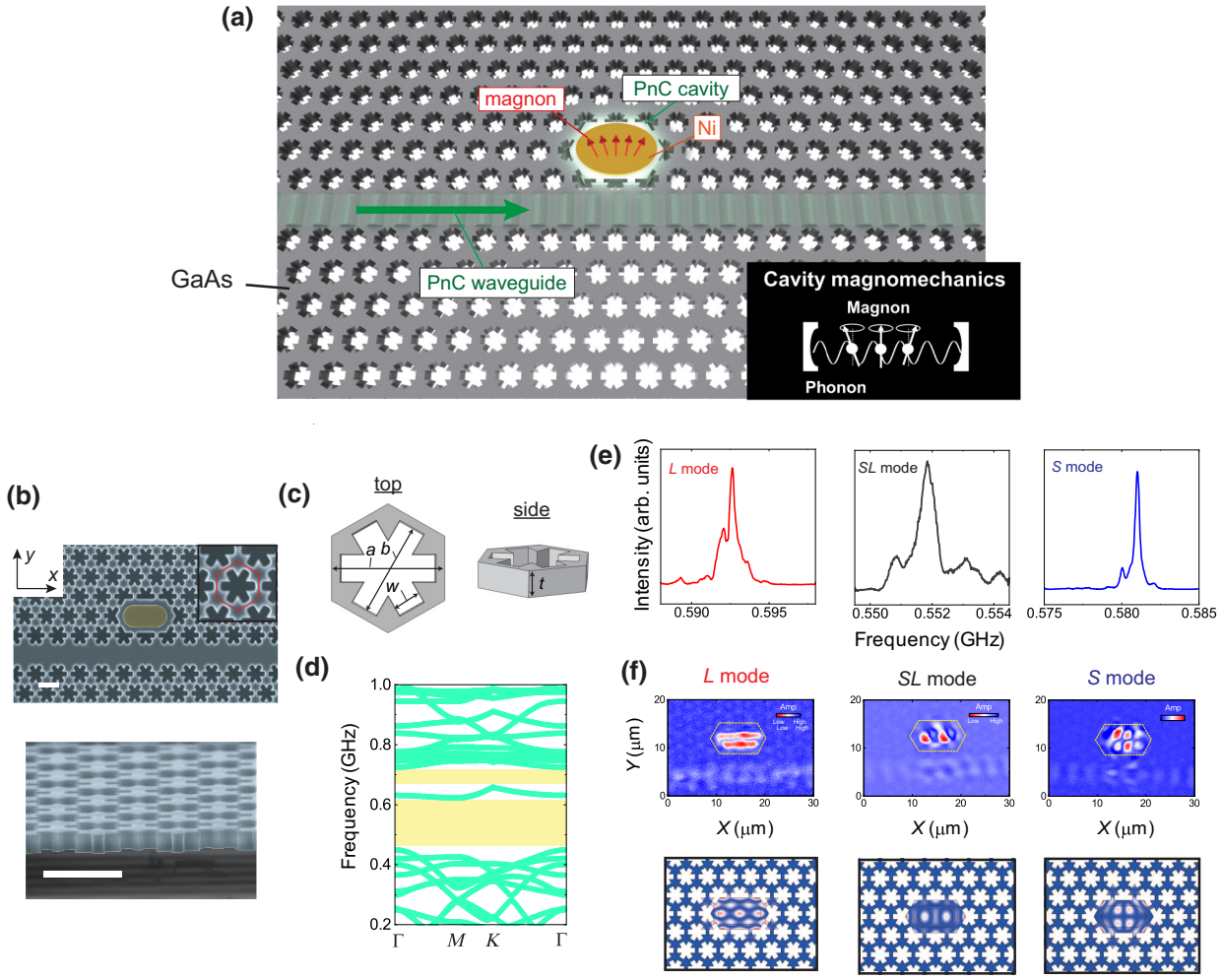

FIG. 1. PnC cavity magnomechanics. (a) Schematic diagram of PnC magnomechanical system and cavity magnomechanical model (inset). The device consists of a GaAs/$Al_{0.7}Ga_{0.3}As$ heterostructure and the PnC is formed in a free-standing GaAs membrane. Rayleigh SAWs are excited by applying an alternating voltage via the piezoelectric effect to interdigit transducers (IDTs) and they transform into asymmetric Lamb waves in the PnC membrane. The acoustic waves excite a PnC cavity resonance through a line-defect waveguide, and the resonant vibrations are measured by an optical interferometer at room temperature and in a moderate vacuum. A ferromagnetic Ni film deposited on the cavity sustains magnon oscillations that are driven by cavity vibrations via magnetostriction. (b) Electron microscope images of the magnomechanical cavity-waveguide geometry (top) and cross section (bottom). The scale bar is 4 μm. The PnC cavity is formed by removing two air holes from the phononic lattice. The Ni film on the defect is false colored in yellow. The inset is an enlargement of the snowflake lattice, and the red solid line denotes the unit structure. (c) Unit cell of PnC lattice designed with $a = 4.0$ μm, $b = 3.6$ μm, $w = 1.0$ μm, and $t = 1.0$ μm. (d) Dispersion relation of the snowflake PnC lattice numerically calculated in FEM (COMSOL MULTIPHYSICS) by applying a periodic boundary condition in the unit cell in (c). A complete phononic band gap forms between 0.42 and 0.72 GHz, except around 0.62–0.66 GHz (highlighted in yellow). (e) Spectral response of the PnC cavity obtained by exciting from the waveguide and measuring the vibration amplitude with an optical interferometer. The y axis is the squared value of the amplitude. From left to right: well-defined acoustic resonance peaks appear at 0.593 GHz (L mode), 0.552 GHz (SL mode), and 0.581 GHz (S mode) with quality factors $Q_a = 550$, 680, and 1540. (f) Experimental (top) and simulated (bottom) modal shape of displacement amplitude of L, SL, and S modes in the left, middle, and right panels. The spatial mode profiles are obtained by scanning the optical laser in the device while exciting the PnC cavity resonances. The PnC cavity geometry is denoted by the dashed yellow lines.

[Fig. 1(e)] whose modal shapes exhibit complete confinement of the vibrations in the defect [Fig. 1(f)]. Numerical calculations with the finite-element method (FEM) reproduced these modal shapes and verified the origin of the observed peaks. We numerically evaluate their effective mode volume and for example, the phononic cavity mode volume at the resonance frequency $\omega_a/(2\pi) = 0.581$ GHz is estimated to be $V_a = 15\ \mu m^3 = 1.2\lambda^2 t (= 0.35\lambda^3)$, with PnC thickness $t = 1.0$ μm and acoustic wavelength $\lambda = 3.5$ μm, while maintaining a high acoustic quality factor of $Q_a = 1\,540$ despite the Ni film loaded on it. This indicates that our system achieves drastic enhancement in Q_a/V_a,

which is 10^4–10^5 times higher than that of a conventional SAW-based magnomechanical system ($V_a = 3.0 \times 10^4\lambda^3$) [31], and enables wavelength-scale ferromagnetic magnons to be acoustically driven. Thus, the PnC enables remote driving of high quality and tiny vibrations and will be a powerful basis for a cavity magnomechanical system.

B. Magnetostriction

The Ni film on the PnC cavity surface has magnetization whose precession is acoustically excited via magnetostriction. The magnetostrictive excitation dynamics are governed by several parameters, such as magnetization direction and spatial strain distribution. We here first summarize their theoretically expected role in the coupled system. The magnetostrictive force that induces the precession is divided into two components $\mu_0 h_1^{\rm am}$ and $\mu_0 h_2^{\rm am}$ on the 1 and 2 axis, whose definitions are given in Fig. 2(a). The equilibrium magnetization axis (m_3) can be decomposed into in-plane x and y components and is at an angle (ϕ_m) from the waveguide direction x. The out-of-plane magnetostrictive force ($\mu_0 h_1^{\rm am}$) is negligibly small because out-of-plane shear strains such as ϵ_{xz} and ϵ_{yz} vanish in the Ni at that location, whereas in-plane force ($\mu_0 h_2^{\rm am}$) can be expressed as [26]

$$\mu_0 h_2^{\rm am} = b_{\rm am}\{(\epsilon_{xx} - \epsilon_{yy})\sin 2\phi_m - 2\epsilon_{xy}\cos 2\phi_m)\}, \quad (1)$$

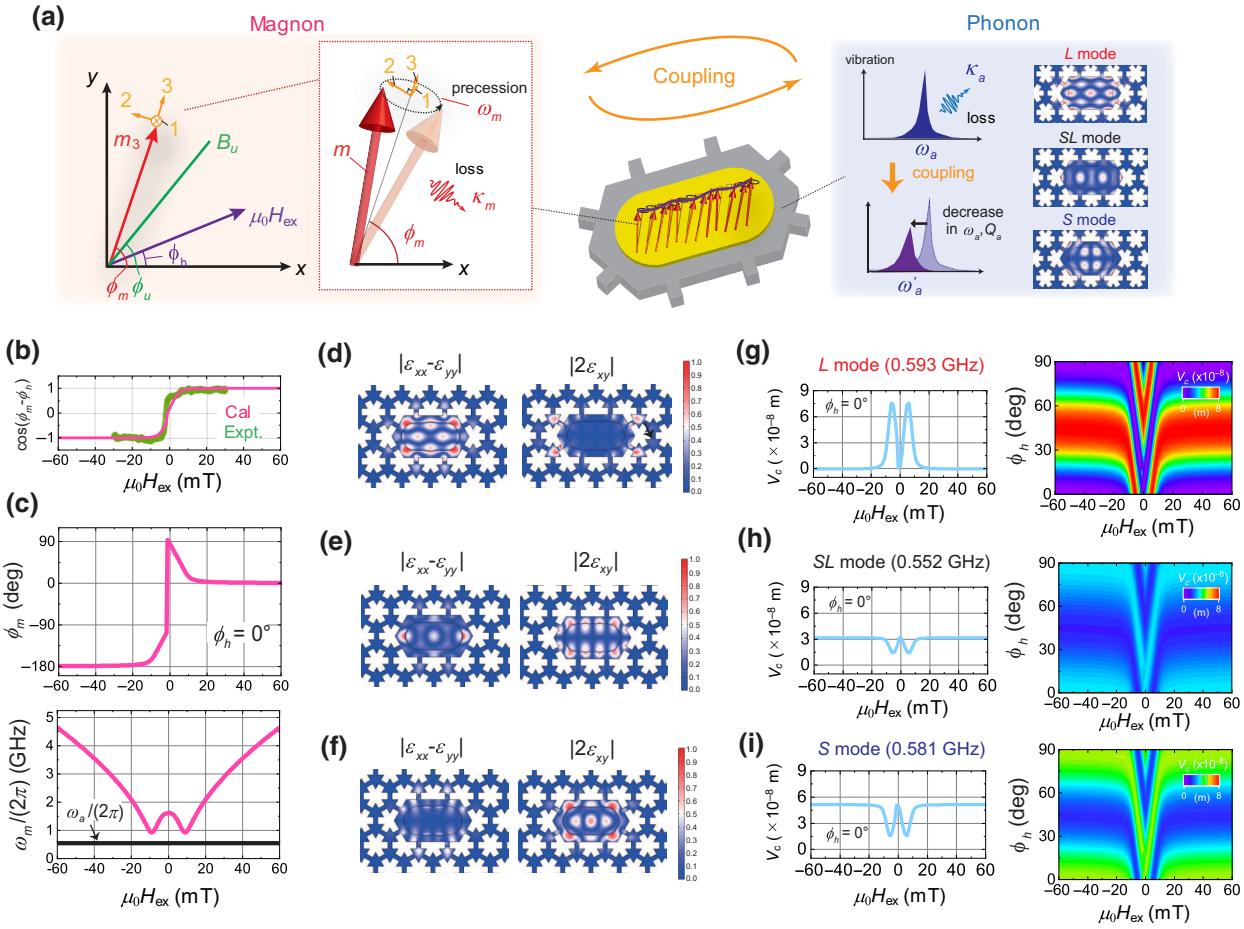

FIG. 2. Magnon-phonon interaction. (a) Left: xy-coordinate system in which the external magnetic field ($\mu_0 H_{\rm ex}$), magnetization (m_3), and in-plane anisotropic field (B_u), respectively, have an angle of ϕ_h, ϕ_m, and ϕ_u away from the x axis. The inset shows the alternative 1-, 2-, and 3-axis coordinate system. The 1 and 2 axis define the magnetization precession plane normal to the 3 axis. The spin oscillation with frequency ω_m and damping κ_m is sustained by the Ni thin film. Right: acoustic resonant vibrations in the PnC cavity whose frequency and quality factor change due to magnetostrictive coupling. (b) Equilibrium magnetization component projected to the field orientation at $\phi_h = 0^\circ$ plotted as a function of the bias field ($\mu_0 H_{\rm ex}$); the green and pink solid lines are experimental and calculated results. The magnetization versus $\mu_0 H_{\rm ex}$ curve is obtained by magneto-optical Kerr microscopy. (c) (top) Field dependence of the magnetization angle (ϕ_m); (bottom) spin-wave resonance frequency ($\omega_m/(2\pi)$). The black solid line in the bottom panel is the acoustic resonant frequency ($\omega_a/(2\pi)$). (d)–(f) Spatial distribution of strain components $|\epsilon_{xx} - \epsilon_{yy}|$ (left) and $|2\epsilon_{xy}|$ (right) in L [0.593 GHz, (d)], SL [0.552 GHz, (e)], and S (0.581 GHz) modes simulated by FEM. The color scales of the SL and S modes are normalized by the maximum strain of $|2\epsilon_{xy}|$, and that of the L mode by $|\epsilon_{xx} - \epsilon_{yy}|$. (g)–(i) Left: field response of magnetoelastic mode coupling (V_c) at $\phi_h = 0^\circ$. Right: ϕ_h dependence of V_c versus $\mu_0 H_{\rm ex}$ response.

where b_{am} is the magnetostrictive coefficient and ϵ_{ij} is the vibrational strain component. Thus, the phononic excitation efficiency of magnons is governed by two major factors, vibrational strain (ϵ_{xx}, ϵ_{yy} and ϵ_{xy}) and the magnetization direction (ϕ_m), so the competition between the magnitude of these strains determines the magnetic anisotropy of the phononic structure.

C. Magnetization dynamics

The magnetization angle (ϕ_m) can be predicted from the magnetic free-energy density normalized by the saturation magnetization (M_s), given by [26]

$$G = -\mu_0 \mathbf{H}_{\mathrm{ex}} \cdot \mathbf{m} - B_u(\mathbf{m} \cdot \mathbf{u})^2 + B_d m_z^2, \tag{2}$$

where $\mu_0 \mathbf{H}_{\mathrm{ex}}$ and $\mathbf{m}$ are the external magnetic field and unit vector of magnetization, respectively. The thin-film structure of the Ni results in a perpendicular shape anisotropy (B_d). The angle ϕ_m is determined by estimating the minimum of G. In this calculation, the in-plane anisotropic field (B_u) and its unit vector ($\mathbf{u}$) are introduced so as to reproduce the experimental magnetization curve [Fig. 2(b)]. The detailed parameters used in the calculation are shown in Table I in the Appendix. For instance, the response of ϕ_m as a function of $\mu_0 H_{\mathrm{ex}}$ at $\phi_h = 0^\circ$ is shown in the top panel of Fig. 2(c). The magnetization is parallel to $\mu_0 H_{\mathrm{ex}}$, i.e., $\phi_m = 0^\circ$, when the field strength stays in the high field region $|\mu_0 H_{\mathrm{ex}}| > 20$ mT. However, it undergoes a rotation to $\phi_m = 90^\circ$ in the low field region $|\mu_0 H_{\mathrm{ex}}| <$ 20 mT before reversing. In this way, the magnetization experiences a rotation and reversal while sweeping $\mu_0 H_{\mathrm{ex}}$. This change in magnetization determines the magnon resonance frequency ($\omega_m/(2\pi)$). The field response is shown in the bottom panel of Fig. 2(c). The frequency monotonically decreases with decreasing $\mu_0 H_{\mathrm{ex}}$ and approaches the acoustic resonant frequency ($\omega_a/(2\pi)$) at $|\mu_0 H_{\mathrm{ex}}| = 7$ mT, where the magnon-phonon frequency mismatch is minimized.

D. Magnon-phonon spatial mode overlap

Another aspect determining the magnetostriction is the spatial distribution and direction of vibration strains. The observed acoustic resonances can be decomposed into three strain components and Fig. 2(d)–2(f) shows the spatial profiles of the longitudinal ($|\epsilon_{xx} - \epsilon_{yy}|$) and shear strain components ($|2\epsilon_{xy}|$) of the resonances. Shear (longitudinal) strain is dominant in the resonances at 0.581 GHz (0.593 GHz), whereas both strains are comparable at 0.552 GHz. The desired strain distributions can thus be generated by selectively actuating an appropriate resonance. Hereafter, the shear- and longitudinal-strain modes are labeled S and L, while the mode with comparable strains is labeled SL.

The magnetization dynamics and spatial strain profiles allow us to estimate the magnetostrictive coupling mode volume (V_c), which characterizes the interaction efficiency and is determined by magnon-phonon spatial mode overlap. It is given by

$$V_c = \int_V d^3\mathbf{r}\boldsymbol{\Psi}(\mathbf{r}) \cdot \mathbf{v}_{\mathrm{am}}, \tag{3}$$

where $\Psi(\mathbf{r})$ is spatial profile of normalized acoustic displacement amplitude and $\mathbf{v}_{\mathrm{am}}$ is magnetoelastic vector dependent on ϕ_m and the spatial profile of magnons (detailed expression and derivation in the Appendix). Figures 2(g)–2(i) show the simulated field dependence of V_c of the L, SL, and S modes at $\phi_h = 0^\circ$ and for various ϕ_h between 0° and 90°, where the calculations of $\Psi(\mathbf{r})$ and $\mathbf{v}_{\mathrm{am}}$ use the FEM results of Fig. 2(d)–2(f). For the L mode at $\phi_h = 0^\circ$, V_c mostly vanishes in the high field region because $\phi_h = \phi_m = 0^\circ$ and $|2\epsilon_{xy}|$ is negligibly small. In contrast, it increases dramatically as $\mu_0 H_{\mathrm{ex}}$ decreases below 20 mT. This enhancement at $\mu_0 H_{\mathrm{ex}} = 6$ mT is caused by the magnetization rotation from $\phi_m = 0^\circ$ to 45°; thereby, the term $(\epsilon_{xx} - \epsilon_{yy}) \sin 2\phi_m$ becomes nonzero. V_c temporarily returns to almost zero as ϕ_m reaches 90° just before the magnetization reverses and then approaches the original value after the increase at $\phi_m = 225^\circ$ and $\mu_0 H_{\mathrm{ex}} = -6$ mT. In contrast, the S mode exhibits the opposite field dependency, in which a finite V_c in the high field region is reduced in the low field region because the dominant magnetostrictive term is $2\epsilon_{xy} \cos 2\phi_m$, not $(\epsilon_{xx} - \epsilon_{yy}) \sin 2\phi_m$. Clearly, these different magnetic anisotropy comes from the sine and cosine dependence in Eq. (1), where longitudinal strain and shear strain are dominant in the L mode and the S mode, respectively. Since the SL mode has almost equal contributions from both strain components, the variation with respect to $\mu_0 H_{\mathrm{ex}}$ is moderate compared with the other two modes. Thus, these simulations using the coupling mode volume (V_c) can predict the magnetic interaction with inhomogeneously distributed strains in the PnC cavity, where the cavity mode structures as well as the external field can be used to tune the magnetostrictive interaction.

E. External field response of PnC cavity resonances

To experimentally show the magnetostrictive interaction, the field response of the PnC cavity resonance was measured at $\phi_h = 0^\circ$. The $\mu_0 H_{\mathrm{ex}}$ dependence of the acoustic resonance at 0.581 GHz is shown in Fig. 3(a), where the vibrations are clearly suppressed in the low field region $|\mu_0 H_{\mathrm{ex}}| < 20$ mT. This can be caused by the energy absorption to drive the magnon. Comparison between the acoustic spectra at $\mu_0 H_{\mathrm{ex}} = 60$, 30, and 11 mT also reveals the resonant frequency changes with sweeping $\mu_0 H_{\mathrm{ex}}$ as shown in Fig. 3(b). To obtain a deep insight into the phenomenon, the observed resonant frequency shift

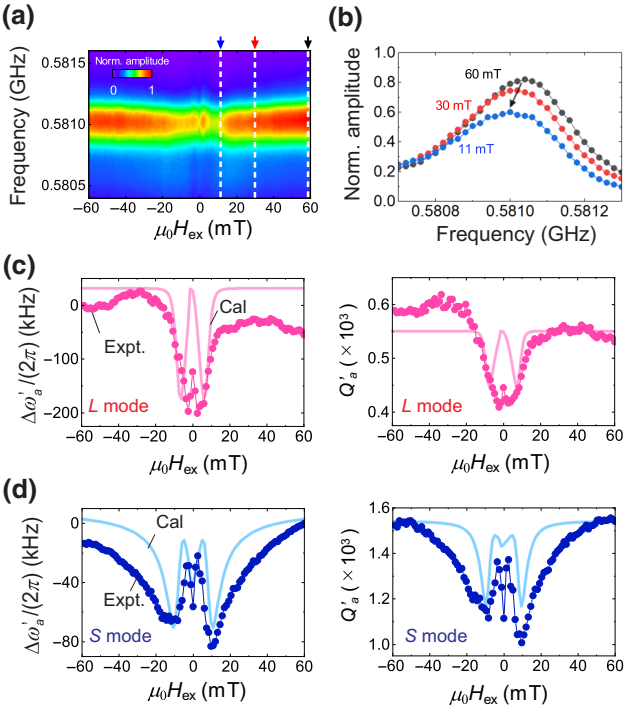

FIG. 3. Magnetoelastic modulation of acoustic cavity resonances. (a) $\mu_0 H_{ex}$ dependence of an acoustic cavity resonant spectrum on S mode. (b) Frequency response of normalized acoustic vibrations in S mode at $\mu_0 H_{ex} = 60$ (black), 30 (red), and 11 mT (blue), denoted by dashed white lines in (a). (c),(d) $\mu_0 H_{ex}$ response of $\Delta\omega_a'/(2\pi)$ (left) and Q_a' (right) in L and S modes at $\phi_h = 0°$. Here, $\Delta\omega_a' = \omega_a' - \omega_{a0}$ where ω_a' is resonant frequency modulated by the magnetoelastic effect and ω_{a0} is the frequency at $|\mu_0 H_{ex}| = 60$ mT. The solid circles are experimental data taken from a Lorentzian fitting to the measured phononic cavity spectra. The solid lines are theoretical results based on Eq. (4).

$(\Delta\omega_a'/(2\pi))$ and quality factor (Q_a') are plotted as a function of $\mu_0 H_{ex}$ in Figs. 3(c) and 3(d), where L and S modes are chosen for their opposite and distinct field susceptibilities, respectively. The response on the L mode exhibits dual dips at $|\mu_0 H_{ex}| = 5$ mT with a reduction in $\Delta\omega_a'/(2\pi)$ and Q_a' [Fig. 3(c)]. This behavior can be understood from the theoretical formula for acoustic displacement amplitude $u_a(\omega)$,

$$u_a(\omega) = \frac{f_d}{-\omega^2 + \omega_a^2 - i\kappa_a\omega + V_c b_{am}^2 \chi_m(\omega)/(\rho V_a)}, \quad (4)$$

where ρ, f_d, and ω are mass density, driving force density, and angular frequency, and χ_m is magnetic susceptibility (see Appendix). The calculation results reproduce the experimental ones, indicating that the acoustic modulation is due to the magnon-phonon interaction, as described by our model. A slight discrepancy between them might be caused by contributions from dipole interaction and multidomain formation in the fabricated Ni film to the magnon dynamics, but we ignore them in the calculations for simplicity. This interaction forms hybridized modes between magnons and phonons and enables acoustic excitation of spin-wave oscillations in Ni and modulation in the acoustic cavity resonance ω_a' and Q_a', whose phenomena are analogous to those observed in microwave cavity magnonics [7].

Remarkably, ferromagnetic magnons are able to be driven by phonons in the wavelength-scale PnC cavity. The tiny-energy vibrations are confined by the high-Q resonance, so they hardly affect surrounding systems, unlike conventional electromagnetic-wave-based magnetic devices. We believe that the PnC cavity-waveguide system would be a building block for a magnomechanical system and could be used as a local magnon driver and phonon modulator.

The magnon-phonon hybridization is also observed in the S mode, where shear strain dominates magnetostriction. A comparison with the effect in the L mode reveals the impact of the mode strain profiles on the interaction. Figure 3(d) shows that the dual dips in this mode at $|\mu_0 H_{ex}| = 10$ mT are wider than those in the L mode because of the finite V_c in the high field region. In addition, a distinct center dip occurs around $\mu_0 H_{ex} = -1$ mT, an effect of the magnetization rotation. The field response is distinctly different from that in the L mode and can be simulated with our model. Thus, our PnC cavity geometry is also used to selectively drive the magnetization dynamics utilizing the difference in strain distributions.

To further examine how the strain distribution affects the magnetoelastic modulation, the field responses of the acoustic resonant frequency $(\Delta\omega_a'/(2\pi))$ and damping rate (κ_a') on the L and S modes are investigated at ϕ_h ranging from 0° to 90° [Figs. 4(a)–4(d)]. The magnetoelastic modulation regions in $\Delta\omega_a'$ and κ_a' broaden as ϕ_h increases from 0° to 50° in the L mode and shrink toward $\phi_h = 90°$. In contrast, the S mode shows the opposite dependency, in which the modulation regions become narrow around $\phi_h = 45°$. The theoretical calculations reproduce the experimental variations in both modes. Here, the cyclic modulations in $\Delta\omega_a'/(2\pi)$ and κ_a' at $\mu_0 H_{ex} = \pm 12$ mT while changing ϕ_h are governed by V_c, so the L and S modes show the opposite behaviors [Figs. 4(e) and 4(f)]. The results reveal that the magnetoelastic anisotropy with respect to $\mu_0 H_{ex}$ and ϕ_h can be tailored by exciting an appropriate PnC cavity mode. It should be also noted that the experiment and theoretical model show a moderate response to the magnetoelastic effect in the SL mode (see Appendix), supporting the validity of our model. We also find similar mode-sensitive magnetoelastic modulation in a PnC cavity with a three-hole defect that is different geometry from the current device (see Appendix). These results verify that the mode-tunable magnetostriction allows us to control magnomechanical states acoustically.

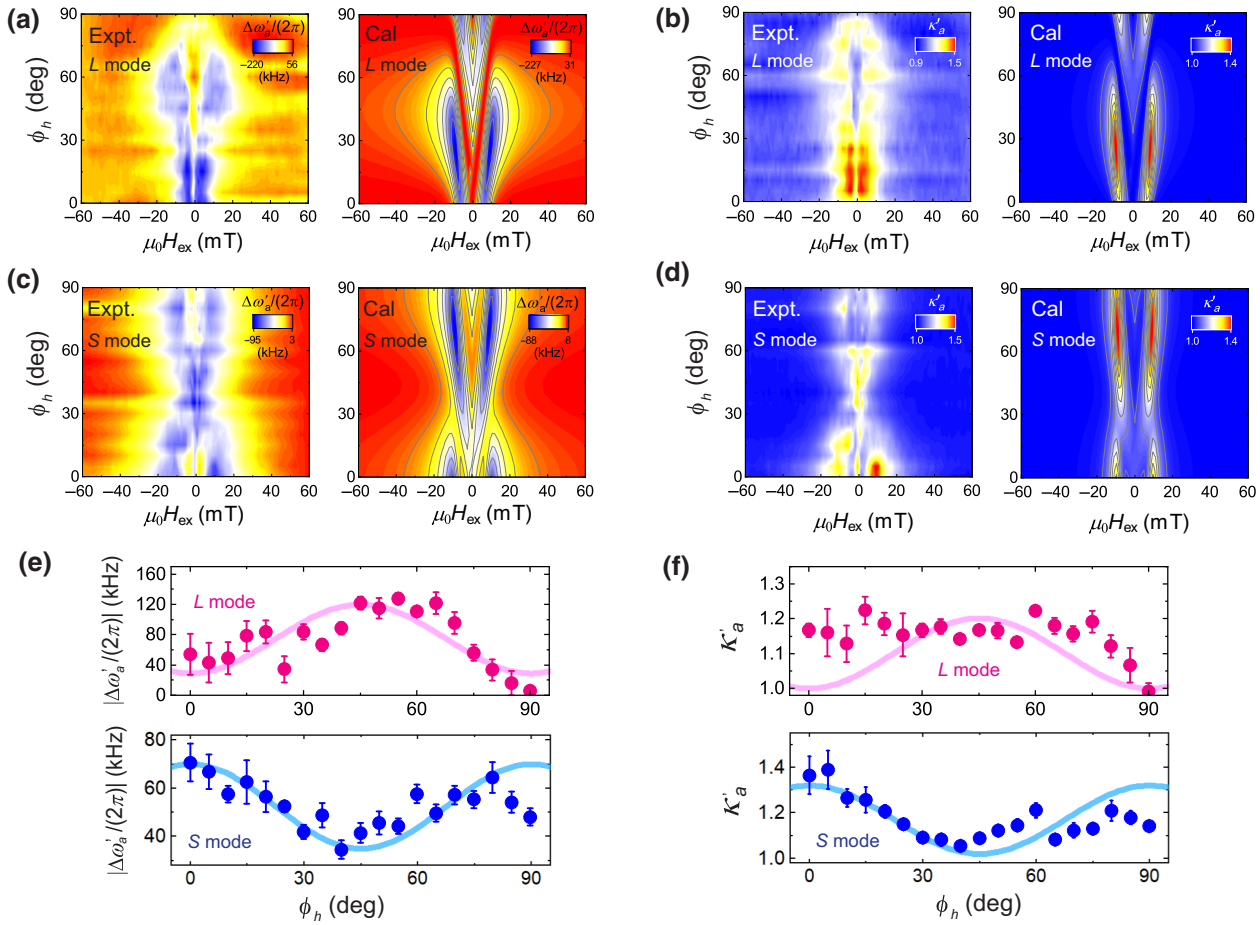

FIG. 4. Magnetoelastic modulation of acoustic cavity to the field orientation. (a)–(d) Field angle (ϕ_h) response of the resonant frequency shift ($\Delta\omega_a'$) and normalized acoustic damping (κ_a') of L and S modes, where the normalized acoustic damping is defined as $\kappa_a' = \kappa_a/\kappa_{a0}$ where κ_{a0} is the value at $|\mu_0 H_{ex}| = 60$ mT. The left and right panels of each figure are experimental and calculated results. Here, we use κ_a' but not Q_a' in order to compare only the magnetoelastic hybridization effects between different ϕ_h. (e),(f) The frequency shift and acoustic damping around $|\mu_0 H_{ex}| = 12$ mT as a function of ϕ_h on the L (top) and S (bottom) modes, respectively. The solid red and blue lines are $(\sin 2\phi_h)^2$ and $(\cos 2\phi_h)^2$ guided by eyes. A slight deviation in the experiment results might be a result of inhomogeneous formation of multidomains and self-dipole interaction in the fabricated Ni film.

III. CONCLUSION

In conclusion, the ease of designing the PnC cavity and the small spatial leakage of its vibrations are useful for constructing integrated magnomechanical circuitry, in which high-tunability, nonlinearity, and nonvolatility of magnons can be used to dynamically control microwave phonons and enables a variety of phononic signal processing, such as amplification, nonreciprocal transport, and nonvolatile switch. Moreover, it is possible to build a tiny magnomechanical system of magnon wavelength size to efficiently control and readout the magnetic state of a micro- and nanoferromagnetic system, such as a magnetic tunnel junction [35]. We believe that cavity magnomechanics empowered by PnC technology will expand the use of magnons, phonons and their interaction for material characterization and signal processing technologies.

ACKNOWLEDGMENTS

This work is partially supported by JSPS KAKENHI(S) Grant No. JP21H05020.

APPENDIX A: FABRICATION AND MEASUREMENT

The magnomechanical PnC is fabricated from GaAs(1.0 μm)/$Al_{0.7}Ga_{0.3}As$(3.0 μm) heterostructure on a GaAs single-crystal substrate. A periodic arrangement of snowflake-shaped air holes is formed by electron-beam lithography and dry etching. The GaAs layer, including the PnC lattice, is suspended by immersion in diluted hydrofluoric acid (5 %). The PnC geometry gives rise to a complete band gap between 0.42–0.62 and 0.66–0.72 GHz. The acoustic waveguide is constructed by removing one line from the lattice, thereby enabling single-mode propagation

at frequencies within the band gap [24]. The acoustic resonator (cavity) formed by removing two holes is located at one side of the waveguide and sustains multiple resonant vibrations. A ferromagnetic thin film of nickel (Ni) with a thickness of 50 nm is deposited on the surface of the PnC cavity and holds spin-wave (magnon) resonances. 5-nm-thick gold (Au) film is deposited on the Ni layer for preventing oxidization. The free-standing PnC slab is sandwiched by interdigit transducers made from Cr(5 nm)/Au(35 nm). The IDT consists of 100 transducers arrayed with a period of 4.9–5.2 μm.

Acoustic waves are piezoelectrically excited by applying alternating voltages to one IDT and optically measured with an optical interferometer (Neoark, MLD-101). The data on the spectral response of the PnC cavity are obtained with a time-gating technique with a network analyzer (Keysight E5080A) to remove undesired electrical crosstalk signals. The acoustic resonance frequencies ($\omega_a'/(2\pi)$) and quality factor (Q_a') in Figs. 3(c) and 3(d) are obtained by making Lorentzian or exponential fittings to the spectral and temporal response results. The acoustic damping rates (κ_a, κ_{a0}) in Figs. 4(b) and 4(d) are estimated from both ω_a' and Q_a'. The displacement amplitudes of the resonant mode profiles depicted in Fig. 1(f) are collected through frequency down-conversion followed by filtering with a lock-in amplifier (Stanford Research Systems, SR844). All experiments in this work are performed in a moderate vacuum (10–100 Pa) and at room temperature.

APPENDIX B: THEORY OF MAGNETOELASTIC DYNAMICS IN A PHONONIC CRYSTAL CAVITY

The equation of motion of the acoustic mode is given by

$$\rho\left(\ddot{u}_i + \kappa_a \dot{u}_i + \omega_a^2 u_i\right) = \partial_{x_k}\sigma_{ik} = \sum_{k=\{x,y,z\}} M_s \partial_k \partial_{\epsilon_{ik}} G_d, \tag{B1}$$

where

$$G_d = \sum_{l,n=\{x,y,z\}} b_{\rm am}\epsilon_{ln} m_l m_n \tag{B2}$$

is the magnetoelastic energy density. The magnetoelastic force density in the second term on the right-hand side is given by

$$f_{{\rm am},i} \equiv \sum_k M_s \partial_k \partial_{\epsilon_{ik}} G_d = M_s b_{\rm am} \sum_{k,l,n} \delta_{li}\delta_{nk}\partial_k m_l m_n = M_s b_{\rm am}(\nabla \cdot m_i \mathbf{m}). \tag{B3}$$

In our setup, the magnetization is aligned in plane of the Ni film and the field angle away from the x axis is defined as ϕ_m. Therefore, the conversion between xyz-coordinate system and 123-coordinate system is

$$\begin{pmatrix} m_x \\ m_y \\ m_z \end{pmatrix} = \begin{pmatrix} 0 & -\sin\phi_m & \cos\phi_m \\ 0 & \cos\phi_m & \sin\phi_m \\ -1 & 0 & 0 \end{pmatrix} \begin{pmatrix} m_1 \\ m_2 \\ m_3 \end{pmatrix}, \tag{B4}$$

$$m_x = -\sin\phi_m m_2 + \cos\phi_m \tag{B5}$$

$$m_y = \cos\phi_m m_2 + \sin\phi_m \tag{B6}$$

$$m_z = -m_1 \tag{B7}$$

with approximations $m_1, m_2 \ll m_3 \sim 1$. Accordingly, under shear strains $\epsilon_{iz} \approx \epsilon_{zi} \approx 0$, the magnetostrictive force density in Eq. (B3) becomes

$$f_{{\rm am},x}/(M_s b_{\rm am}) = \sum_k \partial_k m_x m_k = -\sin 2\phi_m \partial_x m_2 + \cos 2\phi_m \partial_y m_2 + \mathcal{O}(m_i^2) \tag{B8}$$

and

$$f_{{\rm am},y}/(M_s b_{\rm am}) = \sum_k \partial_k m_y m_k = \cos 2\phi_m \partial_x m_2 + \sin 2\phi_m \partial_y m_2 + \mathcal{O}(m_i^2), \tag{B9}$$

where $f_{{\rm am},x}$ and $f_{{\rm am},y}$ are the x and y components of the magnetostrictive force. As a result, we can define an alternative magnetoelastic vector,

$$\mathbf{v}_{\rm am} \equiv \frac{\mathbf{f}_{\rm am}}{M_s b_{\rm am}} = \begin{pmatrix} -\sin 2\phi_m & \cos 2\phi_m \\ \cos 2\phi_m & \sin 2\phi_m \end{pmatrix} \nabla \Phi_{m_2}(\mathbf{r}) \tag{B10}$$

where $\Phi_{m_2}(\mathbf{r})$ is the normalized amplitude of magnons at position $\mathbf{r}$. This magnetoelastic vector contributes to the coupling constant with the spatial integration of magnons. By redefining the acoustic mode as $\mathbf{u}(\mathbf{r}, t) = U_a(t)\boldsymbol{\Psi}(\mathbf{r})$, we find that

$$\ddot{U}_a(t) + \kappa_a \dot{U}_a(t) + \omega_a^2 U_a(t) = M_s b_{\rm am} \frac{\int d\mathbf{r}\boldsymbol{\Psi}(\mathbf{r})\cdot\mathbf{v}_{\rm am}}{\int d\mathbf{r}\rho(\mathbf{r})|\boldsymbol{\Psi}(\mathbf{r})|^2} m_2(t) \equiv M_s b_{\rm am}\frac{V_{c0}}{m_{\rm eff}} m_2(t), \tag{B11}$$

where

$$m_{\rm eff} \equiv \rho V_a = \rho \int_V d^3\mathbf{r}|\boldsymbol{\Psi}(\mathbf{r})|^2 \tag{B12}$$

is the effective mass with $\max_{\mathbf{r}}\left[|\boldsymbol{\Psi}(\mathbf{r})|^2\right] = 1$ and

$$V_{c0} = \int_V d^3\mathbf{r}\boldsymbol{\Psi}(\mathbf{r})\cdot\mathbf{v}_{\rm am} \tag{B13}$$

is the magnetostrictive coupling mode volume. Note that $\Phi_{m_2}(\mathbf{r})$ and $m_2(t)$ are nondimensional variables.

1. Equation of motion for magnon modes

The previous work by Dreher *et al.* [26] derived the following equations of magnonic motion:

$$\frac{\alpha}{\gamma}\dot{m}_1 + (G_{11} - G_3)m_1 - \frac{1}{\gamma}\dot{m}_2 = 0, \tag{B14}$$

$$\frac{\alpha}{\gamma}\dot{m}_2 + (G_{22} - G_3)m_2 + \frac{1}{\gamma}\dot{m}_1 = b_{\mathrm{am}}\left[\sin 2\phi_{\mathrm{m}}(\partial_x u_x - \partial_y u_y) - \cos 2\phi_{\mathrm{m}}\left(\partial_y u_x + \partial_x u_y\right)\right]. \tag{B15}$$

To determine Ψ_{m_i}, we have to diagonalize Eqs. (B14) and (B15),

$$\dot{m}_1 = G_1\alpha m_1 + G_2 m_2 + \frac{\gamma}{1+\alpha^2}F_{\mathrm{am}}, \tag{B16}$$

$$\dot{m}_2 = -G_1 m_1 + G_2\alpha m_2 + \frac{\gamma\alpha}{1+\alpha^2}F_{\mathrm{am}}, \tag{B17}$$

where $G_i \equiv \gamma(G_3 - G_{ii})/(1+\alpha^2)$ and $F_{\mathrm{am}} = b_{\mathrm{am}}\left[\sin 2\phi_{\mathrm{m}}(\partial_x u_x - \partial_y u_y) - \cos 2\phi_{\mathrm{m}}\left(\partial_y u_x + \partial_x u_y\right)\right]$. Here $G_{11} = 2B_d$, $G_{22} = -2B_u \sin^2(\phi_{\mathrm{m}} - \phi_u)$, and $G_3 = -\mu_0 H_{\mathrm{ex}}\cos(\phi_{\mathrm{m}} - \phi_h) - 2B_u\cos^2(\phi_{\mathrm{m}} - \phi_u)$. Finally, we obtain

$$\begin{pmatrix}\dot{m}_+\\ \dot{m}_-\end{pmatrix} = \begin{pmatrix}\lambda_+ & 0\\ 0 & \lambda_-\end{pmatrix}\begin{pmatrix}m_+\\ m_-\end{pmatrix} + \frac{\gamma}{1+\alpha^2}F_{\mathrm{am}}P^{-1}\begin{pmatrix}1\\ \alpha\end{pmatrix}, \tag{B18}$$

where

$$\lambda_\pm \equiv \frac{\alpha(G_1+G_2) \mp \sqrt{-2G_1G_2(2+\alpha^2) + (G_1^2+G_2^2)\alpha^2}}{2} \tag{B19}$$

and

$$\frac{\gamma}{1+\alpha^2}F_{\mathrm{am}}P^{-1}(1,\alpha)^T \equiv (s_+, s_-)^T\frac{\gamma}{1+\alpha^2}F_{\mathrm{am}}. \tag{B20}$$

s_+ and s_- are defined as

$$s_+ = -i\frac{G_1(2+\alpha^2) - G_2\alpha^2 + \alpha\sqrt{G_1^2\alpha^2 + G_2^2\alpha^2 - 2G_1G_2(2+\alpha^2)}}{2\sqrt{G_1^2\alpha^2 + G_2^2\alpha^2 - 2G_1G_2(2+\alpha^2)}}, \tag{B21}$$

$$s_- = i\frac{G_1(2+\alpha^2) - G_2\alpha^2 - \alpha\sqrt{G_1^2\alpha^2 + G_2^2\alpha^2 - 2G_1G_2(2+\alpha^2)}}{2\sqrt{G_1^2\alpha^2 + G_2^2\alpha^2 - 2G_1G_2(2+\alpha^2)}}. \tag{B22}$$

As a result, the equations of magnon motion becomes

$$\dot{m}_\pm = \lambda_\pm m_\pm + \frac{\gamma s_\pm}{1+\alpha^2}F_{\mathrm{am}}. \tag{B23}$$

By decomposing the temporal and spatial parts as $m_\pm \to m_\pm(t)\Phi_\pm(\mathbf{r})$, it can be expressed as

$$\dot{m}_\pm(t)\Phi_\pm(\mathbf{r}) = \lambda_\pm m_\pm(t)\Phi_\pm(\mathbf{r}) + \frac{b\gamma s_\pm}{1+\alpha^2}U(t)\left[\sin 2\phi_m\left(\frac{\partial\Psi_x}{\partial x} - \frac{\partial\Psi_y}{\partial y}\right) - \cos 2\phi_m\left(\frac{\partial\Psi_x}{\partial y} + \frac{\partial\Psi_y}{\partial x}\right)\right] \tag{B24}$$

and

$$\Phi_+(\mathbf{r}) = \Phi_-(\mathbf{r}) = \frac{1}{K}\left[\sin 2\phi_m(\partial_x\Psi_x - \partial_y\Psi_y) - \cos 2\phi_m\left(\partial_y\Psi_x + \partial_x\Psi_y\right)\right], \tag{B25}$$

where K is a wave vector defined as $K \equiv \max_{\boldsymbol{r}}\left[\sin 2\phi_{\mathrm{m}}(\partial_x\Psi_x - \partial_y\Psi_y) - \cos 2\phi_{\mathrm{m}}\left(\partial_y\Psi_x + \partial_x\Psi_y\right)\right]$. Accordingly, the diagonalized equations can be simplified to

$$\dot{m}_\pm(t) = \lambda_\pm m_\pm(t) + \frac{b\gamma s_\pm K}{1+\alpha^2}U(t). \tag{B26}$$

Of note, we have the relationship

$$\begin{pmatrix} m_+ \\ m_- \end{pmatrix} = \frac{1}{i}\begin{pmatrix} -\frac{(G_1-G_2)\alpha-\sqrt{-2G_1G_2(2+\alpha^2)+(G_1^2+G_2^2)\alpha^2}}{2G_1} & -\frac{(G_1-G_2)\alpha+\sqrt{-2G_1G_2(2+\alpha^2)+(G_1^2+G_2^2)\alpha^2}}{2G_1} \\ 1 & 1 \end{pmatrix}^{-1}\begin{pmatrix} m_1 \\ m_2 \end{pmatrix} \tag{B27}$$

and thus, we use

$$m_2 \approx i(m_+ + m_-). \tag{B28}$$

2. Coupled mode equation

The above equations of motions of acoustic phonons and magnons lead to the following equation of motion of coupled modes:

$$\ddot{U}_a(t) + \kappa_a \dot{U}_a(t) + \omega_a^2 U_a(t) = iM_s b_{\rm am}\frac{V_c}{Km_{\rm eff}}\left(m_+(t) + m_-(t)\right) \tag{B29}$$

$$\dot{m}_\pm(t) = \lambda_\pm m_\pm(t) + \frac{b_{\rm am}\gamma s_\pm K}{1+\alpha^2}U_a(t), \tag{B30}$$

where the coupling mode volume is redefined as $V_c = \int_V d^3\mathbf{r}\boldsymbol{\Psi}(\mathbf{r})\cdot\mathbf{v}_{\rm am}$ and

$$\mathbf{v}_{\rm am} = \frac{1}{2}\begin{pmatrix} -\nabla^2\Psi_x + \cos 4\phi_m\left(\partial_x^2\Psi_x - \partial_y^2\Psi_x - 2\partial_x\partial_y\Psi_y\right) + \sin 4\phi_{\rm m}\left(\partial_x^2\Psi_y - \partial_y^2\Psi_y + 2\partial_x\partial_y\Psi_x\right) \\ -\nabla^2\Psi_y + \cos 4\phi_m\left(\partial_y^2\Psi_y - \partial_x^2\Psi_y - 2\partial_x\partial_y\Psi_x\right) + \sin 4\phi_m\left(\partial_x^2\Psi_x - \partial_y^2\Psi_x - 2\partial_x\partial_y\Psi_y\right) \end{pmatrix}. \tag{B31}$$

By solving Eqs. (B29) and (B30) with an additional driving force, f_d, we obtain the acoustic displacement amplitude ($U_a(t) = u_a e^{i\omega t}$) modulated by the magnetoelastic hybridization, where

$$u_a(\omega) = \frac{f_d}{-\omega^2 + \omega_a^2 - i\kappa_a\omega + V_c b_{\rm am}^2\chi_m(\omega)/(\rho V_a)}, \tag{B32}$$

and the magnetic susceptibility is

$$\chi_m(\omega) = -i\frac{M_s\gamma}{1+\alpha^2}\left(\frac{s_-}{-i\omega - i\omega_m + \frac{\kappa_m}{2}} + \frac{s_+}{-i\omega + i\omega_m + \frac{\kappa_m}{2}}\right). \tag{B33}$$

For the numerical calculation, we had to derive the value of $\sqrt{V_c/m_{\rm eff}}$ at which the spatial function appears as the same order $|\Psi|^2$. This means that constant factors cancel out in their ratio. Magnetoelastic coupling coefficients ($b_{\rm am}$) of 5, 6, and 10 T are used for the simulations of the *SL*, *S*, and *L* modes, respectively. The angle of the in-plane anisotropic field was set at $\Delta\phi_u = \phi_u - \phi_h = 85^\circ$, to reproduce the field response of the equilibrium magnetization as shown in Fig. 2(b). The table lists the other parameters of the calculations.

By transforming into the rotating frame of the acoustic modes, i.e., $U_a(t) = Ae^{-i\omega_a t}$, the equation of motion of acoustic phonons becomes

$$\dot{A} + \frac{\kappa_a}{2} = -\frac{M_s b_{\rm am} V_c}{2\omega_a K m_{\rm eff}}\left(m_+(t) + m_-(t)\right). \tag{B34}$$

The coupled mode equation in the frequency domain is given by

$$\begin{pmatrix} -i\omega + \frac{\kappa_a}{2} & +\frac{M_s b_{\rm am} V_c}{2\omega_a K m_{\rm eff}} & \frac{M_s b_{\rm am} V_c}{2\omega_a K m_{\rm eff}} \\ -\frac{b_{\rm am}\gamma s_+ K}{1+\alpha^2} & -i\omega - \lambda_+ & 0 \\ -\frac{b_{\rm am}\gamma s_- K}{1+\alpha^2} & 0 & -i\omega - \lambda_- \end{pmatrix}\begin{pmatrix} U_a(\omega) \\ m_+(\omega) \\ m_-(\omega) \end{pmatrix} \equiv \begin{pmatrix} -i\omega + \frac{\kappa_a}{2} & G_{A+} & G_{A-} \\ -G_{+A} & -i\omega - \lambda_+ & 0 \\ -G_{-A} & 0 & -i\omega - \lambda_- \end{pmatrix}\begin{pmatrix} U_a(\omega) \\ m_+(\omega) \\ m_-(\omega) \end{pmatrix} = \begin{pmatrix} f_d \\ 0 \\ 0 \end{pmatrix}.$$

TABLE I. Acoustic and magnetic parameters used in the calculations.

ρ	Mass density	8900 kg/m^3
B_d	Out-of-plane shape anisotropy	0.2 T
B_u	In-plane magnetic anisotropy	4 mT
α	Gilbert damping factor	0.1
M_s	Saturation magnetization	370 kA/m
γ	Gyromagnetic ratio	2.185 $\mu_B/\hbar$

Hence, the acoustic mode spectra is

$$U_a(\omega) = f_d\left[-\frac{G_{A+}G_{+A}}{(\lambda_+ + i\omega)} - \frac{G_{A-}G_{-A}}{(\lambda_- + i\omega)} + (-i\omega + \frac{\kappa_a}{2})\right]^{-1}. \tag{B35}$$

Apparently, the symmetrized coupling strength is

$$G_{\pm} \equiv \sqrt{G_{A\pm}G_{\pm A}} = b_{\rm am}\sqrt{\frac{M_s\gamma s_{\pm}}{2\omega_a\left(1+\alpha^2\right)}}\sqrt{\frac{V_c}{m_{\rm eff}}}. \tag{B36}$$

APPENDIX C: MAGNETOELASTIC MODULATION OF *SL* MODE IN A PNC CAVITY

Figure 5(a) plots the resonant frequency shift ($\Delta\omega_a'/(2\pi)$) and quality factor (Q_a') as functions of the bias field ($\mu_0 H_{\rm ex}$) for the *SL* mode in the $\phi_h = 0°$. Their field responses reveal a dual dip structure due to the increased magnon-phonon interaction; the theoretical calculations (solid line) show the same dip. Compared with the other modes, the modulation magnitudes, i.e., dip depths, are small, because of the comparable contributions of the longitudinal ($|\epsilon_{xx} - \epsilon_{yy}|$) and shear strain components ($|2\epsilon_{xy}|$), and thus, the field angle dependency of the coupling (V_c) is relatively moderate as shown in Figs. 5(d) and 5(e). Figures 5(b) and 5(c) show the experimental (left) and simulated (right) field responses of $\Delta\omega_a'$ and Q_a' while sweeping ϕ_h from 0° to 90°. The field regions of the magnetoelastic modulation exhibit moderate variation with ϕ_h compared with the *S* and *L* modes. Clearly, the magnetoelastic dynamics are a consequence of the spatial strain distribution of this mode.

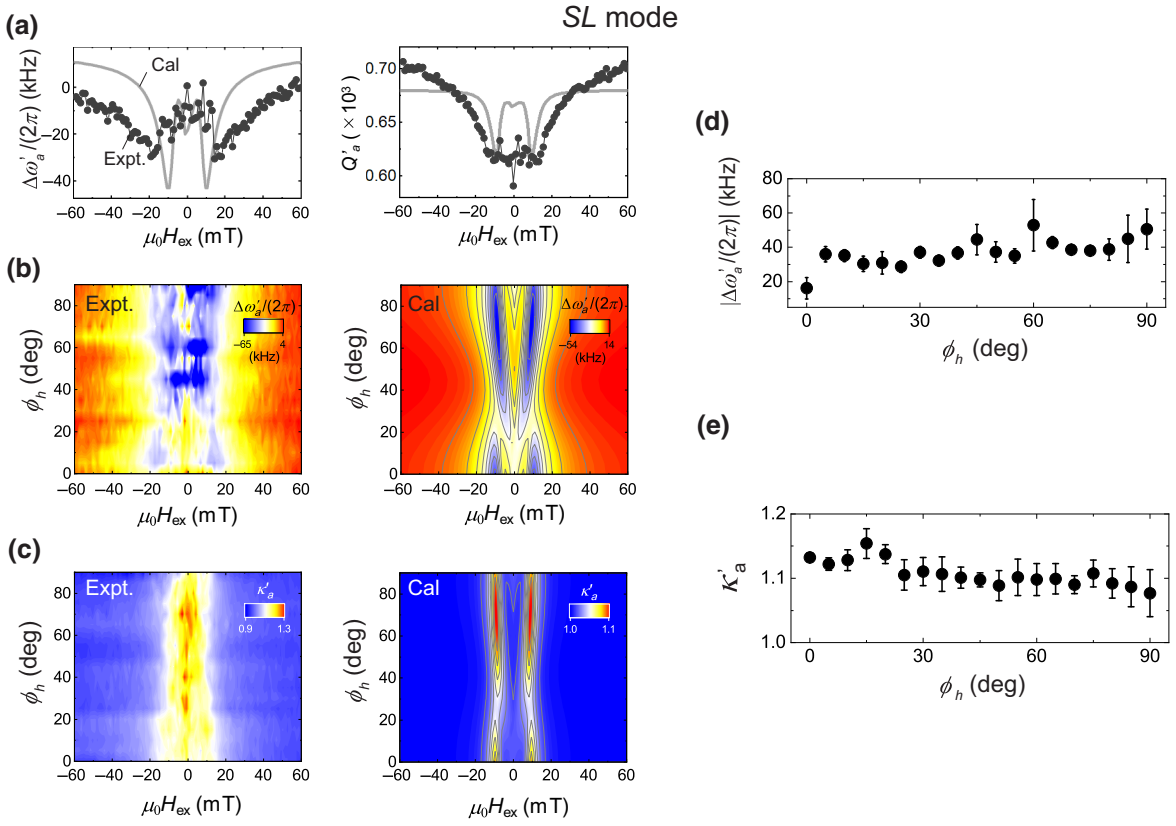

FIG. 5. Magnetoelastic modulation on an acoustic resonance of *SL* mode. (a) The field ($\mu_0 H_{\rm ex}$) dependence of resonant frequency shift ($\Delta\omega_a'/(2\pi)$) and quality factor (Q_a') at $\phi_h = 0°$ in the left and right panels, respectively. (b),(c) The ϕ_h dependence of the frequency $\Delta\omega_a'/(2\pi)$ and damping κ_a' versus $\mu_0 H_{\rm ex}$, respectively. The experimental and calculated results are shown in the left and right panels. (d),(e) The ϕ_h dependence of $|\Delta\omega_a/(2\pi)|$ and κ_a' at $|\mu_0 H_{\rm ex}| = 12$ mT.

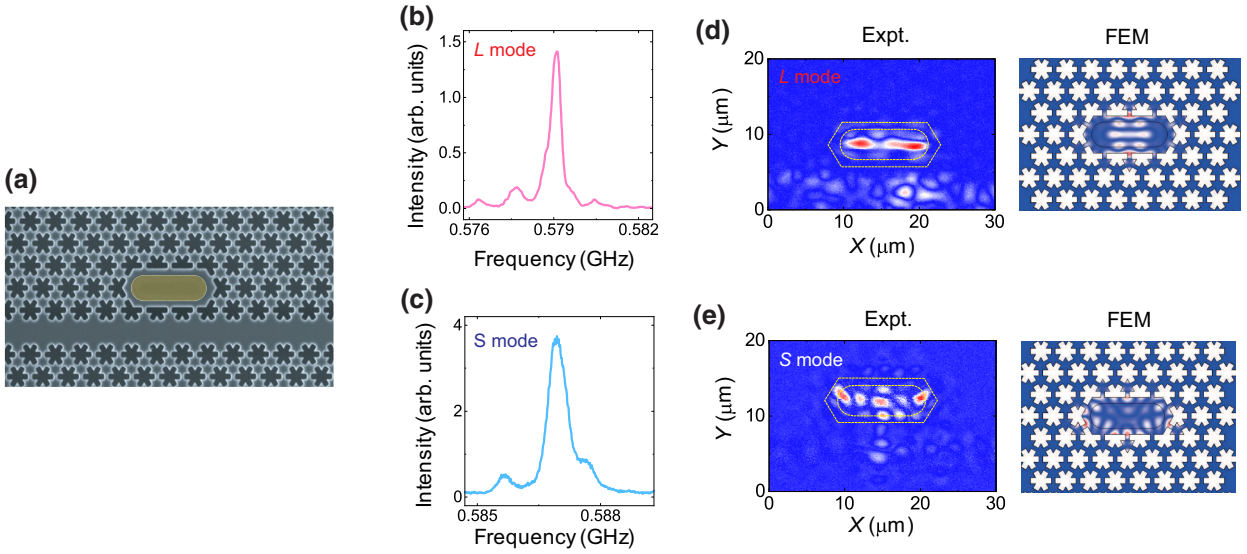

FIG. 6. Acoustic dynamics of PnC cavity with three hole defect. (a) SEM image of the PnC cavity coupled to a waveguide. A Ni film (yellow) is placed on the surface of the PnC cavity. (b),(c) Acoustic resonant spectrum of L and S modes. (d),(e) Experimental (left) and calculated (right) spatial profiles of the resonant vibration amplitude in L and S modes. The defect region is highlighted by yellow dotted lines in the left panel.

APPENDIX D: MAGNETOELASTIC MODULATION ON A PNC CAVITY WITH A THREE-HOLES DEFECT

A PnC cavity formed by removing three holes, shown in Fig. 6(a), has two acoustic resonances at 0.579 and 0.587 GHz with distinct modal shapes [Figs. 6(b) and 6(c)]. These modes, labeled L and S, indicate that acoustic vibrations are confined in the defect [Figs. 6(d) and 6(e)]. Figures 7(a) and 7(b) plot the numerically calculated spatial distributions of strains $|\epsilon_{xx} - \epsilon_{yy}|$ and $|2\epsilon_{xy}|$, while Figs. 7(c) and 7(d) plot the magnetoelastic coupling mode volume V_c as a function of the bias field strength $\mu_0 H_{\mathrm{ex}}$ at $\phi_h = 0°$. These field responses indicate that the two modes show opposite coupling dynamics. Similarly, the field angle evolution of the V_c response indicates the magnetoelastic modulation effect is sensitive to the field and magnetization orientation and the acoustic mode structure [right panels of Figs. 7(c) and 7(d)]. Figures 8(a) and 8(c) indicate the frequency shifts of the L and S modes (left) and simulated responses (right), while Figs. 8(b) and 8(d) plot the normalized acoustic damping rates (left) and the simulated responses (right). Figures 8(e) and 8(f) show the field angle dependence of $|\Delta\omega_a'/(2\pi)|$ and normalized

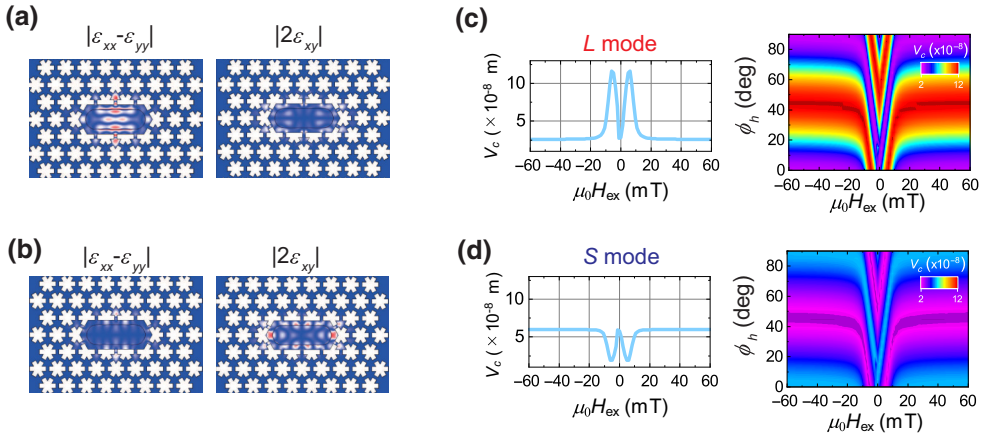

FIG. 7. Spatial strain profiles of PnC cavity resonances and their magnetoelastic coupling mode volume. (a),(b) Spatial distribution of longitudinal $|\epsilon_{xx} - \epsilon_{yy}|$ (left) and shear $|2\epsilon_{xy}|$ (right) strains on L and S modes, respectively. (c),(d) Left: simulated magnetoelastic coupling mode volume (V_c) as a function of field strength ($\mu_0 H_{\mathrm{ex}}$) at $\phi_h = 0°$. Right: corresponding field angle (ϕ_h) dependence of $V_c - \mu_0 H_{\mathrm{ex}}$.

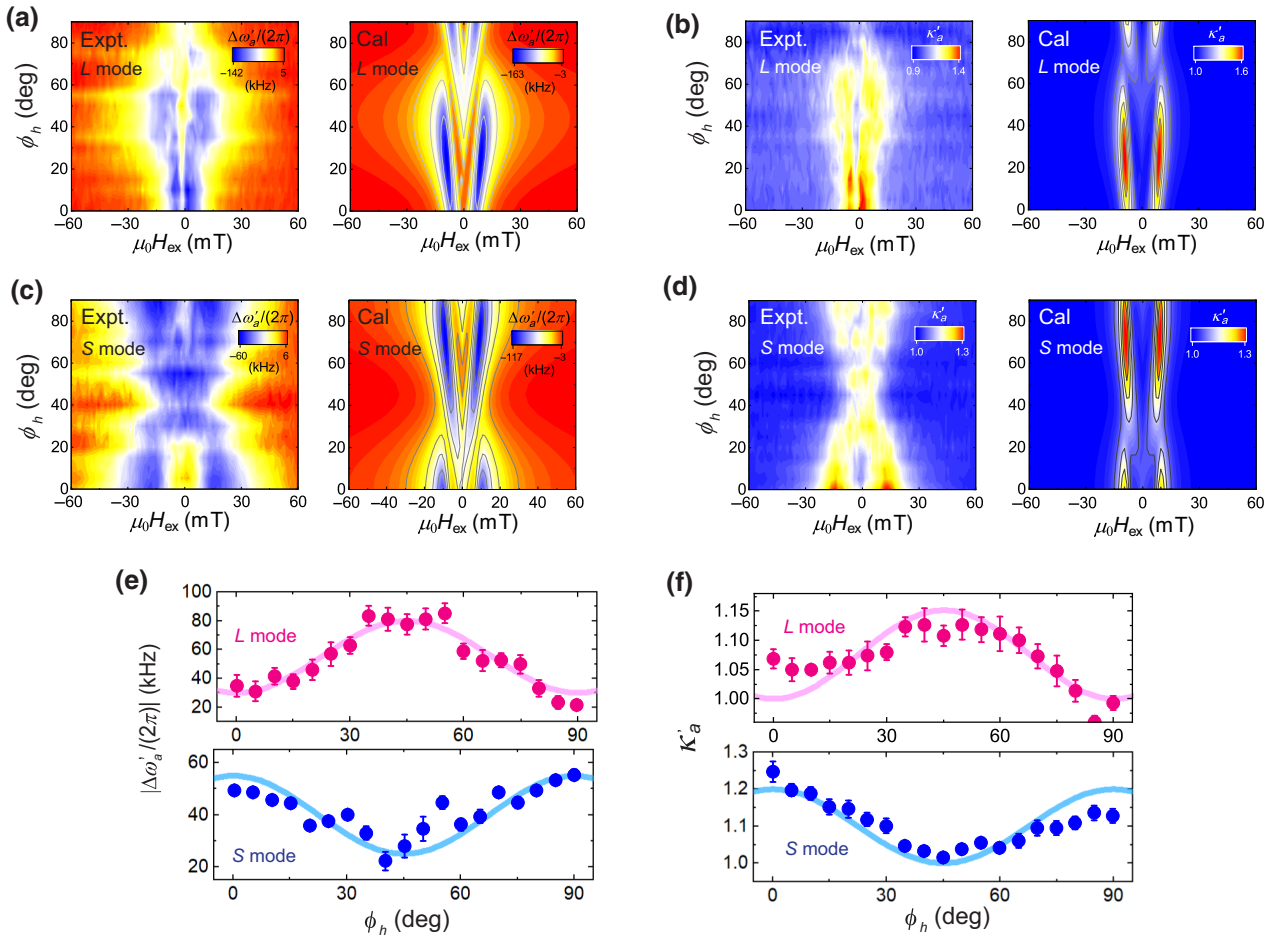

FIG. 8. Mode-sensitive magnetoelastic cavity dynamics. (a)–(d) Experimental (left) and simulated (right) ϕ_h dependence of $\Delta\omega_a'/(2\pi)$ (a),(c) and κ_a' (b),(d) as a function of $\mu_0 H_{\rm ex}$ in L and S modes. (e),(f) The field angle dependence of $\left|\Delta\omega_a'/(2\pi)\right|$ and normalized κ_a' at $|\mu_0 H_{\rm ex}| = 15$ mT on the L (top) and S (bottom) modes are shown, respectively. The solid lines of $(\sin 2\phi_h)^2$ (top) and $(\cos 2\phi_h)^2$ (bottom) are plotted for the comparison.

κ_a' at $|\mu_0 H_{\rm ex}| = 15$ mT on the L (top) and S (bottom) modes. The magnetoelastic coupling coefficient used in the calculations is $b_{\rm am} = 7$ T for both modes.

[1] A. V. Chumak, V. I. Vasyuchka, A. A. Serga, and B. Hillebrands, Magnon spintronics, Nat. Phys. **11**, 453 (2015).

[2] P. Pirro, V. I. Vasyuchka, A. A. Serga, and B. Hillebrands, Advances in coherent magnonics, Nat. Rev. Mater. **6**, 1114 (2021).

[3] J. Torrejon, M. Riou, F. A. Araujo, S. Tsunegi, G. Khalsa, D. Querlioz, P. Bortolotti, V. Cros, K. Yakushiji, A. Fukushima, *et al.*, Neuromorphic computing with nanoscale spintronic oscillators, Nature **547**, 428 (2017).

[4] B. Z. Rameshti, S. V. Kusminskiy, J. A. Haigh, K. Usami, D. Lachance-Quirion, Y. Nakamura, C.-M. Hu, H. X. Tang, G. E. Bauer, and Y. M. Blanter, Cavity magnonics, Phys. Rep. **979**, 1 (2022).

[5] X. Zhang, C.-L. Zou, L. Jiang, and H. X. Tang, Strongly Coupled Magnons and Cavity Microwave Photons, Phys. Rev. Lett. **113**, 156401 (2014).

[6] M. Goryachev, W. G. Farr, D. L. Creedon, Y. Fan, M. Kostylev, and M. E. Tobar, High-Cooperativity Cavity QED with Magnons at Microwave Frequencies, Phys. Rev. Appl. **2**, 054002 (2014).

[7] Y. Tabuchi, S. Ishino, T. Ishikawa, R. Yamazaki, K. Usami, and Y. Nakamura, Hybridizing Ferromagnetic Magnons and Microwave Photons in the Quantum Limit, Phys. Rev. Lett. **113**, 083603 (2014).

[8] Y. Tabuchi, S. Ishino, A. Noguchi, T. Ishikawa, R. Yamazaki, K. Usami, and Y. Nakamura, Coherent coupling between a ferromagnetic magnon and a superconductiong qubit, Science **349**, 405 (2015).

[9] A. Osada, R. Hisatomi, A. Noguchi, Y. Tabuchi, R. Yamazaki, K. Usami, M. Sadgrove, R. Yalla, M. Nomura, and Y. Nakamura, Cavity Optomagnonics with Spin-Orbit Coupled Photons, Phys. Rev. Lett. **116**, 223601 (2016).

[10] Y. Li, C. Zhao, W. Zhang, A. Hoffmann, and V. Novosad, Advances in coherent coupling between magnons and acoustic phonons, APL Mater. **9**, 060902 (2021).

[11] X. Zhang, C.-L. Zou, L. Jiang, and H. X. Tang, Cavity magnomechanics, Sci. Adv. **2**, e1501286 (2016).
[12] H. Walther, B. T. Varcoe, B.-G. Englert, and T. Becker, Cavity quantum electrodynamics, Rep. Prog. Phys. **69**, 1325 (2006).
[13] T. Kikkawa, K. Shen, B. Flebus, R. A. Duine, K.-i. Uchida, Z. Qiu, G. E. Bauer, and E. Saitoh, Magnon Polarons in the Spin Seebeck Effect, Phys. Rev. Lett. **117**, 207203 (2016).
[14] C. Berk, M. Jaris, W. Yang, S. Dhuey, S. Cabrini, and H. Schmidt, Strongly coupled magnon–phonon dynamics in a single nanomagnet, Nat. Commun. **10**, 1 (2019).
[15] K. An, A. N. Litvinenko, R. Kohno, A. A. Fuad, V. V. Naletov, L. Vila, U. Ebels, G. de Loubens, H. Hurdequint, N. Beaulieu, *et al*., Coherent long-range transfer of angular momentum between magnon Kittel modes by phonons, Phys. Rev. B **101**, 060407(R) (2020).
[16] C. A. Potts, E. Varga, V. A. Bittencourt, S. V. Kusminskiy, and J. P. Davis, Dynamical Back Action Magnomechanics, Phys. Rev. X **11**, 031053 (2021).
[17] M. Maldovan, Sound and heat revolutions in phononics, Nature **503**, 209 (2013).
[18] D. Hatanaka, I. Mahboob, K. Onomitsu, and H. Yamaguchi, Phonon waveguides for electromechanical circuits, Nat. Nanotechnol. **9**, 520 (2014).
[19] S. Benchabane, A. Khelif, J.-Y. Rauch, L. Robert, and V. Laude, Evidence for complete surface wave band gap in a piezoelectric phononic crystal, Phys. Rev. E **73**, 065601 (2006).
[20] S. Mohammadi, A. A. Eftekhar, W. D. Hunt, and A. Adibi, High-Q micromechanical resonators in a two-dimensional phononic crystal slab, Appl. Phys. Lett. **94**, 051906 (2009).
[21] P. H. Otsuka, K. Nanri, O. Matsuda, M. Tomoda, D. M. Profunser, I. A. Veres, S. Danworaphong, A. Khelif, S. Benchabane, V. Laude, *et al*., Broadband evolution of phononic-crystal-waveguide eigenstates in real- and k-spaces, Sci. Rep. **3**, 3351 (2013).
[22] R. Pourabolghasem, R. Dehghannasiri, A. A. Eftekhar, and A. Adibi, Waveguiding Effect in the Gigahertz Frequency Range in Pillar-Based Phononic-Crystal Slabs, Phys. Rev. Appl. **9**, 014013 (2018).
[23] M. G. Baboly, C. M. Reinke, B. A. Griffin, I. El-Kady, and Z. C. Leseman, Acoustic waveguiding in a silicon carbide phononic crystals at microwave frequencies, Appl. Phys. Lett. **112**, 103504 (2018).
[24] D. Hatanaka and H. Yamaguchi, Real-Space Characterization of Cavity-Coupled Waveguide Systems in Hypersonic Phononic Crystals, Phys. Rev. Appl. **13**, 024005 (2020).
[25] M. Weiler, L. Dreher, C. Heeg, H. Huebl, R. Gross, M. S. Brandt, and S. T. B. Goennenwein, Elastically Driven Ferromagnetic Resonance in Nickel Thin Films, Phys. Rev. Lett. **106**, 117601 (2011).
[26] L. Dreher, M. Weiler, M. Pernpeintner, H. Huebl, R. Gross, M. S. Brandt, and S. T. B. Goennenwein, Surface acoustic wave driven ferromagnetic resonance in nickel thin films: Theory and experiment, Phys. Rev. B **86**, 134415 (2012).
[27] D. Kobayashi, T. Yoshikawa, M. Matsuo, R. Iguchi, S. Maekawa, E. Saitoh, and Y. Nozaki, Spin Current Generation using a Surface Acoustic Wave Generated via Spin-Rotation Coupling, Phys. Rev. Lett. **119**, 077202 (2017).
[28] R. Sasaki, Y. Nii, Y. Iguchi, and Y. Onose, Nonreciprocal propagation of surface acoustic wave in Ni/$LiNbO_3$, Phys. Rev. B **95**, 020407 (2017).
[29] A. Hernández-Mínguez, F. Macià, J. Hernàndez, J. Herfort, and P. Santos, Large Nonreciprocal Propagation of Surface Acoustic Waves in Epitaxial Ferromagnetic/Semiconductor Hybrid Structures, Phys. Rev. Appl. **13**, 044018 (2020).
[30] M. Xu, K. Yamamoto, J. Puebla, K. Baumgaertl, B. Rana, K. Miura, H. Takahashi, D. Grundler, S. Maekawa, and Y. Otani, Nonreciprocal surface acoustic wave propagation via magneto-rotation coupling, Science Adv. **6**, eabb1724 (2020).
[31] D. Hatanaka, M. Asano, H. Okamoto, T. Kunihashi, H. Sanada, and H. Yamaguchi, On-Chip Coherent Transduction Between Magnons and Acoustic Phonons in Cavity Magnomechanics, Phys. Rev. Appl. **17**, 034024 (2022).
[32] T. Kawada, M. Kawaguchi, T. Funato, H. Kohno, and M. Hayashi, Acoustic spin Hall effect in strong spin-orbit metals, Sci. Adv. **7**, eabd9697 (2021).
[33] H. Matsumoto, T. Kawada, M. Ishibashi, M. Kawaguchi, and M. Hayashi, Large surface acoustic wave nonreciprocity in synthetic antiferromagnets, Appl. Phys. Express **15**, 063003 (2022).
[34] A. H. Safavi-Naeini, J. T. Hill, S. Meenehan, J. Chan, S. Gröblacher, and O. Painter, Two-Dimensional Phononic-Photonic Band Gap Optomechanical Crystal Cavity, Phys. Rev. Lett. **112**, 153603 (2014).
[35] S. Yuasa, T. Nagahama, A. Fukushima, Y. Suzuki, and K. Ando, Giant room-temperature magnetoresistance in single-crystal Fe/MgO/Fe magnetic tunnel junctions, Nat. Mater. **3**, 868 (2004).